Kühn, D., Heimann, S., Isken, M. P., Ruigrok, E., Dost, B. (2020): Probabilistic Moment Tensor Inversion for Hydrocarbon-Induced Seismicity in the Groningen Gas Field, The Netherlands, Part 1: Testing. - Bulletin of the Seismological Society of America, 110, 5, 2095-2111.

https://doi.org/10.1785/0120200099

Probabilistic moment tensor inversion for hydrocarbon-induced seismicity in the Groningen gas field, the Netherlands, part 1: testing

D. Kühn[1,2*] S. Heimann[2] M. P. Isken[3,2]
E. Ruigrok[4] B. Dost[4]

[1] NORSAR, Applied Seismology, Kjeller, Norway
[2] GFZ German Research Centre for Geosciences, Physics of Earthquakes and Volcanoes, Potsdam, Germany
[3] Christian-Albrechts-University, Department of Geosciences, Kiel, Germany
[4] Royal Netherlands Meteorological Institute (KNMI), De Bilt, The Netherlands

July 1, 2020

Abstract

Since 1991, induced earthquakes have been observed and linked to gas production in the Groningen field. Recorded waveforms are complex, resulting partly from a Zechstein salt layer overlying the reservoir

*corresponding author: daniela@norsar.no

and partly from free-surface reverberations, internal multiples, interface conversions, guided waves and waves diving below the reservoir. Therefore, picking of polarities or amplitudes for use in moment tensor inversion is problematic, whereas phase identification may be circumvented employing full waveform techniques. While moment tensors have become a basic tool to analyse earthquake sources, their uncertainties are rarely reported. We introduce a method for probabilistic moment tensor estimation and demonstrate its use on the basis of a single event within the Groningen field, concentrating on detailed tests of input data and inversion parameters to derive rules of good practice for moment tensor estimation of events recorded in the Groningen field. In addition to the moment tensor, event locations are provided. Hypocentres estimated simultaneously with moment tensors are often less sensitive to uncertainties in crustal structure, which is pertinent for the application to the Groningen field, since the task of relating earthquakes to specific faults hitherto suffers from a limited resolution of earthquake locations. Due to the probabilistic approach, parameter trade-offs, uncertainties and ambiguities are mapped. In addition, the implemented bootstrap method implicitly accounts for modelling errors affecting every station and phase differently. A local 1D velocity model extracted from a full 3D velocity model yields more consistent results than other models applied previously. For all velocity models and combinations of input data tested, a shift in location of 1 km to the south is observed for the test event compared to the public catalogue. A full moment tensor computed employing the local 1D velocity model features negative isotropic components and may be interpreted as normal fault and collapse at reservoir level.

Keywords— p robabilistic – moment tensor inversion – induced seismicity – Groningen gas field

Introduction

Since 1991, induced earthquakes have been observed and linked to the gas production in the Groningen field (for a detailed description of seismicity, see e.g., Dost et al., 2017). Despite the relatively low magnitude of earthquakes, their impact is considerable due to their shallow origin and the presence of soft shallow sediments that amplify wave motion (Paap et al., 2018). Events with magnitudes $M_L > 2$ are commonly felt and larger earthquakes have damaged buildings and thus, pose a safety hazard to the population (Paap et al., 2018).

Kraaijpoel and Dost (2013) computed focal mechanisms assuming a pure double couple mechanism for four specific events within the western part of the field from P-wave first motion polarities and P/S amplitude ratios. Due to the limited azimuthal coverage of the network before 2015, accelerograms were employed in addition to seismograms. Kraaijpoel and Dost (2013) identified the Zechstein salt layer situated above the reservoir as challenging due to the defocussing of seismic energy and potential presence of strong S-wave precursors. The presence of salt layers is a well-known challenge for imaging and interpretation in reflection seismology (Ogilvie and Purnell, 1996; Lu et al., 2003) and a similar problem is encountered in earthquake analysis; for instance, for the largest event in the field so far, the M_W 3.6 Huizinge event on August 16, 2012, an attempt was made to recover the focal mechanism, but no stable solution could be found (Dost and Kraaijpoel, 2013). Since 2015, the network was upgraded extensively by introduction of a multitude of shallow borehole stations, which reduced interstation distances considerably (Dost et al., 2017). Nevertheless, even waveforms recorded at small distances are complex due to free surface reverberations, internal multiples, interface conversions (Spetzler and Dost, 2017) as well as guided waves at reservoir level and waves diving below the reservoir (Willacy et al., 2018). Thus, picking of polarities and amplitudes, for example for use in focal mechanism or moment tensor inversion is problematic (Dando et al., 2019), while the use of full waveforms circumvents the problem of phase identification. By this means Willacy et al. (2018, 2019) employed a sophisticated grid search and a 3D velocity model to compute full moment tensors based on the method presented by Li et al. (2016) for 100 events recorded by the shallow borehole network between 2015 and 2017.

While seismic moment tensors have become a basic tool to analyse earthquake sources and are calculated routinely by a number of agencies for global and regional earthquakes, however, parameter uncertainties are still not always provided (Mustać and Tkalčić, 2015). Such uncertainties are important especially in the case of earthquakes with significant non-double couple components since the amount of double couple and isotropic components may vary significantly already for small perturbations of parameters (Zahradnik et al., 2008). In addition, the source location is usually determined by seismic wave arrival times and thus, is identical to the hypocentre - the starting point of the rupture - as opposed to the centroid - the average location of the seismic energy release recovered by moment tensor inversion (Mustać and Tkalčić, 2015). In addition, the location estimate determined from moment tensor inversion, especially its depth, is often less sensitive to uncertainties in crustal structure (Zahradnik et al., 2008). For both reasons, it is advisable to include the centroid earthquake location as parameter in the inversion, especially since for the Groningen field, the task of relating earthquakes to specific faults hitherto suffers from the limited resolution of earthquake locations.

Earthquake source inversions require a comparison between model predictions and observations in a quantitative way. In a well-behaved overdetermined inversion problem, with normally distributed measurement errors and no mismodelling, the choice of how the comparison is done should not influence the result as long as the full information from the observations is included and errors are propagated correctly. In practice, hardly any of the above prerequisites holds and an objective function has to be designed that enhances or extracts robust features of the waveforms and suppresses the parts that cannot be modelled accurately. Typically, waveforms are at least filtered and tapered before fitting to extract specific phases. E.g. Li et al.

(2011) and Tan et al. (2018) show that it can be beneficial to include P-wave polarities and S/P amplitude ratios in addition to waveform fits. Alvizuri et al. (2018) as well include P-wave polarities for very small events. Silwal and Tape (2016) find that using an L1 norm gives more robust results. It depends on application and dataset which approach proves to be best-suited as there is no standard solution. The performance of different objective functions may be compared by quantifying uncertainties.

To this aim, Bayesian or probabilistic inversions are now increasingly being applied in geophysical inversion problems. Probabilistic inversions can be roughly grouped into two families: (1) The problem is formulated directly in terms of Bayes' theorem, such that data and modelling uncertainties enter as a priori information into the inversion (Bayesian inference, popularized in geophysics by Tarantola et al. (1982), applications to point source inversion by e.g. Duputel et al. (2012); Stähler and Sigloch (2014); Mustać and Tkalčić (2015); Gu et al. (2017); Fichtner and Simutė (2018). (2) The problem is expressed indirectly in terms of a stochastic inversion with randomized, re-weighted, or noise-perturbed datasets (jackknife resampling and various types of bootstrapping, see e.g. Wéber (2006); Heimann (2011); the term bootstrap being coined by Efron (1979)). In addition, some authors argue that under certain assumptions, a classic misfit function evaluated on a dense grid around the neighbourhood of a best-fitting solution can be converted into a probability density or confidence function (e.g. Tape and Tape, 2016; Silwal and Tape, 2016; Alvizuri et al., 2018).

Due to the composite nature of linear and non-linear constituents of the centroid moment tensor inversion problem, most probabilistic inversion approaches differ in how they treat centroid locations. For example, Stähler and Sigloch (2014) use a waveform similarity measure based on cross-correlation values in a teleseismic application to be independent of source location. Others, as e.g. Gu et al. (2017), align observed and synthetic traces before a Bayesian inversion or divide the problem into a chain of coupled samplers, e.g. Wéber (2006); Mustać and Tkalčić (2015). Since we apply an inversion to data recorded locally, we expect that by including position and origin time as inversion parameters and by not discarding phase information, the inversion will be constrained better, especially since the azimuth to close-by stations varies significantly depending on source locations.

Within this paper, we introduce a method for probabilistic centroid moment tensor estimation based on the Bayesian bootstrap method (Rubin, 1981) and demonstrate its use on the basis of a single event within the Groningen field, presenting detailed test results of input data types, velocity models, station depths, resolvability of source mechanisms and influence of noise. The use of the bootstrap method to quantify uncertainties enables us to easily combine the fitting of different waveform attributes during the inversion and to employ an L1 norm succeeding in more robust results compared to the L2 norm. Furthermore, the method is easier to handle than applying Bayesian inference with full error propagation, because it does not require noise estimates as prior information. Still, our method is able to effectively account for noise in data and to some extent for mismodelling apart from a systematic bias, since it exploits statistical properties of the residuals. Computational costs are reduced substantially by the implementation of a sophisticated and flexible search algorithm. In a second paper (Dost et al., 2020, this issue), we show the application of the algorithm to events occurring within the Groningen field for the time period January 2016 to July 2019 and give an interpretation of results.

Method

We implemented our inversion using the Grond framework (Heimann et al., 2018), an open source Python software package for probabilistic earthquake source inversion based on the Pyrocko package (Heimann et al., 2017). We compute source model estimates and uncertainties by employing a bootstrap-based probabilistic joint inversion. The optimisation routine offers a flexible design of objective functions, explores the full model space and maps model parameter trade-offs. Forward modelling is accelerated by the use of pre-computed Green's function databases, which are handled by the related Python Pyrocko-GF software library (Heimann et al., 2019). For forward modelling of regional seismological data, the incorporated orthonormal propagator method QSEIS (Wang, 1999) is well suited and used for computation of the Green's function databases in the following.

The misfit between observed and synthetic data is represented by the objective function, whose global minimum is searched during the optimisation process. Input data, weights, norm and error treatment influence the shape of the objective function. We systematically explore different combinations of waveform processing and misfit functions in either time or frequency domain. The misfit is based on the L^p norm and p is set commonly, but is not restricted to, to 1 or 2. Misfits are normalised in groups to enable relative weighting of individual target misfits. By *target* we refer to the contribution of a processed waveform at a given station and component. Pre-processing of waveforms involves the removal of instrument responses, frequency band-limited conversion to displacement and extraction of desired phases by tapering.

We restrict the following explanation to the use of the L^1 norm, which we employed in the inversion. Thus, the normalized global misfit is constructed as

$$M = \frac{\sum_i w_i m_i}{\sum_i w_i n_i} \; , \tag{1}$$

where m_i is the misfit combined from the individual target misfits, n_i is the corresponding normalisation factor, and w_i is the weighting factor discussed below. For time domain- or frequency domain-based misfits, the target misfits and normalisation factors are computed as

$$m_i = \sum_j |o_{ij} - s_{ij}| \qquad \text{and} \qquad n_i = \sum_j |o_{ij}| \; , \tag{2}$$

where o_{ij} is the observed processed sample with index j of target i and s_{ij}

is the corresponding synthetic sample. For cross-correlation based waveform similarity measures, we use instead

$$m_i = \frac{1}{2} - \frac{1}{2} C_i \qquad \text{and} \qquad n_i = \frac{1}{2}\ , \tag{3}$$

where C_i is the maximum of the normalised cross-correlation between the processed traces o_{ij} and s_{ij} in time domain.

To derive the weighting factors in Eq. (1), we employ the product of balancing, manual and bootstrap weights:

$$w_i = w_{\mathrm{balance},i}\, w_{\mathrm{manual},i}\, w_{\mathrm{bootstrap},i}\ . \tag{4}$$

Balancing weights are computed using the adaptive station weighting method of Heimann (2011), which represents a technique to compensate for amplitude variations of seismic waves at different distances due to geometrical spreading, between different phases or introduced by different processing schemes. An additional correction has to be applied when combining misfits based on individual samples with misfits based on cross-correlation, because of their different scaling behaviour with respect to the scalar moment of the source (normalisation families Heimann et al., 2018). Manual weights can be optionally introduced to further tune the objective function based on user experience.

For optimisation, the Bayesian bootstrap optimisation algorithm (BABO, Heimann et al., 2018) is employed. Multiple objective functions M_k are explored in parallel as individual *bootstrap chains*, which allows for a probabilistic interpretation of the result ensemble. During each iteration, an individual misfit is computed for each bootstrap chain. Each bootstrap chain indexed by k differs from the others by an additional random weight factor, the bootstrap weight $w_{\mathrm{bootstrap},ki}$, which is attached to each misfit target i. The bootstrap weights are chosen according to the scheme presented by Rubin (1981), which allows to treat the result ensemble as a non-parametric posterior distribution. In the optimization, an individual highscore list is maintained for each bootstrap chain, holding its current best L models. This list is updated after each iteration, when all objective functions M_k are evaluated for a candidate model. L depends on the number of parameters and a configurable factor, commonly $L > 100$. Bootstrap chains converging to different areas of the model space represent the uncertainty of the models with respect to errors in the data. Once these areas start to become disjunct, further iterations will not significantly improve results and error estimates. From the combination of results from all bootstrap chains' highscore lists, the current best and mean solutions can be retrieved. The optimisation may be tweaked to overcome ill-posed problems or to cover multiple minima of the objective function.

The parameter space is first sampled uniformly followed by a directed search phase; the number of iterations required for each phase depends on the optimisation problem. New models are distributed normally, either centered around the mean of the parameter distribution of the models on the highscore lists, around a random model from the highscore list or from a distribution corrected for excentricity, all with a freely adaptable search radius based on the standard deviation of model parameters in the highscore list. Thus, strictly speaking, since the algorithm searches for minima in the parameter space covered by a high number of forward models, it does not represent an inversion in the mathematical sense. Nevertheless, we will use the term "inversion" in the following in the broader sense of solving an inverse problem. For a more detailed description of the methodology, see Heimann et al. (2018) or the application of the algorithm to events in the region between Halle and Leipzig, Germany (Dahm et al., 2018).

For reproducibility, we provide the Grond input configurations and detailed output reports for all inversion runs in a separate data publication (Kühn et al., 2020).

Data and processing

In order to test inversion parameters, we employed the 11^{th} March 2017 (12:52:48 GMT) event close to the village of Zeerijp, featuring a magnitude of M_L 2.1. This event is located in the central part of the Groningen gas field in the region of maximum compaction due to gas production. The reservoir below Zeerijp is characterized by large lateral differences in net hydrocarbon produced as well as by NNW SSE striking faults identified from detailed 3D seismics (de Jager and Visser, 2017). Zeerijp is among the most seismogenic areas within the Groningen gas field, yielding detectable seismicity from 1996 onwards. The largest event in this region was the 8th January 2018 earthquake featuring a magnitude of M_L 3.4. Thus, the magnitude of the event analysed in this paper is at the lower end of the range of felt events ($M_L >$ 1.8).

Fig. 1a displays the event location together with the stations of the G-network. For the inversion we employed data from stations within a 10 km range, since beyond this distance, direct phases are influenced by the presence of guided waves (Willacy et al., 2018, see also Fig. 2d). Stations within this distance range represented by a diamond did not provide recordings for this event.

Stations

After the occurrence of the largest event in the region of the Groningen field in 2012 close to Huizinge, the monitoring network was substantially extended, adding 70 stations between 2014 and 2016 and resulting in a total of 337 geophones at the end of the year 2016 (Dost et al., 2017). Thus, the average station spacing was condensed from 20 km to below 5 km. Due to the high-noise conditions in the north of the Netherlands, each of these stations consists of four levels of 4.5 Hz geophones with 50 m spacing from 50 - 200 m depth accompanied by a surface accelerometer (Dost et al., 2017).

Sensor orientations were determined using correlations with surface sensors (Hofman et al., 2017) and using a combination of check-shots, local events and ambient explosions (Ruigrok et al., 2019). In addition, we tested the orientation of vertical components employing the PKP-phase of the 3rd January 2017 event south of Fiji islands at 145° distance. Before applying the moment tensor inversion, the P-wave polarization was computed and analysed with regard to the catalogue location of the event. Based on these analyses, depth levels on which the sensor orientation was not well resolved were excluded from the inversion. For two stations (marked by a dark triangle in Fig. 1a), data from only one depth level could be employed. Fig. 1b visualises seismograms recorded at 100 m depth (2nd level). No seismogram is presented for station G11, since only data from its first level was deemed to be of sufficient quality to be included in the inversion. Evaluating the power spectral densities of ambient seismic noise, restituted data recorded on the geophones seems to represent amplitudes well down to frequencies of 0.3 Hz.

Velocity models

For a description of the geological structure as well as a discussion on obtainable information on velocity models and the justification to use locally extracted 1D velocity models, see Dost et al. (2020, this issue). In order to build an average 1D velocity model for station distances up to 10 km from the catalogue event location, 17 1D velocity profiles were extracted from the available 3D velocity model (Romijn, 2017) at regular intervals and the average value of each layer's depth was computed.

Fig. 2a offers an overview over velocity models that were tested for the current event, while Figs. 2b-d demonstrate ray paths traced from a source within the reservoir layer, illustrating differences in wave types to be expected at the recording stations up to source-receiver distances of 10 km. Fig. 2a compares P-wave velocity profiles with a focus on the layers above the reservoir, in which most of the seismicity is assumed to occur. The dashed line corresponds to the average velocity profile used by the Royal Netherlands Meteorological Institute (KNMI) for routine event location in all of Northern Netherlands (denoted "NN" in the following), the dotted line represents the velocity model for Groningen employed by Kraaijpoel and Dost (2013, denoted "KD" in the following) and the solid line is the local 1D velocity model averaged from the 3D velocity model by Romijn (2017). The P-wave velocity of the NN model is monotonically increasing and summarises layers to larger blocks. The KD model follows the local velocity model closely, but possesses a smaller velocity gradient in the overburden and omits two thin high-velocity layers representing an anhydrite floater overlaying the Zechstein evaporites as well as an anhydrite layer at the base of the Zechstein evaporites with a thickness of approximately 50 - 100 m. The reservoir corresponds to the low-velocity layer at approximately 3 km depth. In the NN model, receivers at larger distances than approximately 3.5 km are reached only by wave energy originating from a headwave travelling along the reservoir-overburden boundary. Ray paths in the KD model highlight the strong defocussing of wave energy described by Kraaijpoel and Dost (2013). In the local 1D model, only receivers up to a distance of approximately 2 km are reached by direct waves, whereas receivers at larger distances record energy guided within the high-velocity anhydrite layer at the base of the Zechstein evaporites.

For all three velocity models, Green's functions were computed employing a tapered Heaviside wavelet, a sample rate of 25 Hz and a grid spacing of 50 m allowing for interpolation of Green's functions between nodes. The databases comprise source depths from 1 to 4 km and receiver depths from 0 to 200 m. Further, we supplied an S-wave model to the NN model using the formula by Castagna et al. (1985) that was employed as well by Kraaijpoel and Dost (2013).

Inversion parameters

After testing, the following inversion parameters were employed in the BABO optimisation: the L^1 norm was applied for calculation of the misfit between observed and synthetic data; 100 bootstrap chains were traced; 97 high score models were kept from each bootstrap chain, while models could be shared between chains; 4000 iterations were performed during the uniform sampling of the parameter space; 60 000 further iterations were computed in the directed search phase; new candidate models were selected from a distribution covering the volume of highscore models. This distribution was designed to be roughly flat within the neighbourhood of populated model space (eccentricity compensation, Heimann et al., 2018). The definition of neighbourhood was chosen based on marginal parameter median densities. With such a setup, the BABO algorithm can effectively sample irregularly shaped and multi-minimum objective functions. The explorativeness of the algorithm can be tuned with a scalar factor, which can grow or shrink the neighbourhood volume. We exponentially decreased this factor (scatter scale, Heimann et al., 2018) from 2 to 0.5 during the directed search phase in order to sample more exploratory in the beginning, while converging more effectively at the end of the optimization. The result ensemble was compiled from the 10 best models per bootstrap chain, i.e. 1000 solutions in total. The moment tensor is decomposed according to the Frobenius norm (Silver and Jordan, 1982).

Details on the optimisation setup and complete results can be found in a separate data publication (Kühn et al., 2020), including all information to reproduce the presented solutions.

Probabilistic moment tensor estimation

Unless described differently, we employed the local 1D velocity model during the following tests. Further, if not mentioned otherwise, we inverted for deviatoric moment tensors. To this end, we used both P- and S-phases. Due to the complexity of the waveforms (Fig. 1b), P- and S-wave windows were inverted separately to avoid mismodelling of phases in between both onsets. P-waves were extracted from vertical components, S-waves from transversal components. The additional information content of S-wave windows selected on radial components is low, while at the same time, converted waves arrive shortly after the P-wave onset. In addition, errors in the velocity model affect the radial component much stronger than the transversal component, rendering the inversion unnecessarily difficult. By manual analysis of seismograms both P- and S-wave window length were chosen as 0.5 s, starting with the respective theoretical onsets and allowing for a shift of up to 0.1 s between observed and synthetic waveforms reflecting inaccuracies in the velocity model. P-wave traces (or *targets*) were filtered from 2 to 4 Hz, S-wave traces from 1 to 3 Hz. Due to the complexity of waveforms, S-wave target weights were halved with respect to P-wave targets.

Testing types of input data

From the input data types available in the algorithm, we tested: time traces, amplitude spectra, cross-correlation traces (maximizing the highest cross-correlation value), absolute amplitudes and envelopes. When testing with synthetic data, the mechanism was resolved in all cases with only the inherent inabilities that amplitude spectra, absolute amplitudes and envelopes cannot resolve the ambiguity between compression and dilatation and that cross-correlation traces, since normalised, do not carry information on the magnitude of the event (see also Kühn et al., 2020). Thus, we did not observe intrinsic trade-offs between inversion parameters as described by Cesca et al. (2017) e.g. due to insufficient coverage of azimuths or inclination angles. When tested on observed data, resulting event locations were most consistent when inverting time traces and least consistent when inverting amplitude spectra.

A criterion for the stability of the solution is the coincidence of best and mean solution, which was only the case for the inversion of time traces and cross-correlation traces. A systematic trend between compensated linear vector dipole (CLVD) components and event location as well as CLVD component and individual moment tensor components (mostly m_{nn}, m_{ee}, m_{dd} and m_{ne}) was revealed when inverting only time traces, which could be resolved best by employing cross-correlation traces (Fig. 3). Thus, we concluded that is beneficial to apply a combination of input data. This insight is not new, but the impact of each choice can only be illustrated when employing probabilistic inversion methods allowing for the determination of a multitude of solutions with comparable misfit and thus, a mapping of the their distribution in the inversion parameter space.

Testing all potential combinations of input data types is outside the scope of this paper; instead, we resorted to combinations of time traces with one additional input data set. Again, for synthetic tests, the assumed source mechanism was retrieved well and is not presented here (see instead Kühn et al., 2020). When testing combinations of input data types for observed data, resolved event depths were very consistent. Especially for the combination of time traces and cross-correlation traces, epicentral locations agreed very well in addition and the variation of the CLVD component was reduced substantially, now clustering without exception on the positive CLVD axis (Fig. 4).

In Fig. 4, best double couple mechanisms as derived from the decomposition of the deviatoric moment tensors are displayed in the Hudson diagram, since we believe that this adds additional information to the plots. The algebraic sign and size of isotropic and CLVD part are already indicated by the placement of mechanisms within the Hudson plot's coordinate system and showing the best double couple mechanism as well allows an assessment of its stability or instability.

The combination of time traces with only amplitude spectra on the other hand was not satisfactorily (Fig. 5). The consistency of solutions could be increased again, however, when employing a combination of time traces, cross-correlation traces and amplitude spectra. We settled for this combination of input data for the following inversions.

Testing the resolvability of source mechanisms

To analyse the resolvability of different source mechanism for the field-case source-receiver geometry, we varied the source mechanism in a series of tests inverting synthetic data. In addition to systematically varied mechanisms (Fig. 6), we tested the focal mechanisms retrieved by Kraaijpoel and Dost (2013). Further, we investigated an explosive mechanism as well as 20 double couple and 20 full moment tensors varied randomly as displayed in Fig. 7.

Most mechanisms were retrieved perfectly. Mechanisms marked by a dashed box in Figs. 6 and 7 were found, but their magnitude was underestimated. Only one mechanism was not retrieved (marked by a black box in

Fig. 7). However, if a homogeneous velocity model was employed instead of the local 1D velocity model, magnitudes and mechanisms were computed correctly. The answer to this problem lies in the event depth that was chosen for the synthetic tests: only if the event is located within the basal anhydrite, as was the case for the tests depicted above, the mechanism cannot be resolved. If the depth was changed to any of the other layers, also these mechanisms were retrieved perfectly. From comparing seismograms by forward modelling, we note that the retrieved erroneous mechanism placed at the erroneous event depth results in very similar waveforms as the original source at correct depth. That means that for certain source mechanisms, even a moment tensor inversion employing full waveforms can not differentiate between events within the basal anhydrite and the reservoir. This is an important insight, although from efforts on event location, there are no indications for events occurring within the Zechstein layers (Pickering, 2015; Daniel et al., 2016; Willacy et al., 2018, 2019). Spetzler and Dost (2017) found events near an overlaying brittle anhydrite layer. Applying the same location method in a 3D velocity model, though, all events were located within the reservoir layer (Spetzler and Dost, manuscript in preparation).

Thus, the ambiguity between solutions could potentially be solved by inverting for the strain-based source tensor instead of the stress-based moment tensor, since the amplitude of the observed displacements is related to the displacements or strain at the source while conversion from stress to strain involves material parameters which are discontinuous at interfaces.

Testing station depths

We tested both the usage of data from a single three-component sensor per borehole as well as combinations of data from multiple sensors. Not surprisingly, the resolution was lowest if employing only data from the uppermost borehole sensor at 50 m depth, since it is subjected to the highest noise levels. In case only data from a single sensor was used, the resolution increased for sensors at 100 m and 150 m depth, but surprisingly, it deteriorated again for the sensor at 200 m depth (Fig. 8).

When only data from the sensor at 200 m was used, a second minimum in the objective function indicated larger event depths of approximately 3.6 km. For all runs employing data of single or multiple depth levels, the resulting deviatoric moment tensor was stable with respect to the agreement between best and mean solution, apart from when using only data from the sensor at 150 m depth. Due to the nature of the inversion involving bootstrapping, the resolution increased significantly once data from different depth levels were combined. Furthermore, at single depth levels, interferences between upgoing and free-surface reflected downgoing waves lead to notches in the amplitude spectra. These notches vary with sensor depth and therewith the loss of source information at one depth level is substituted by the information content at a different depth level. Thus, data should not be extracted from either one of these sensor levels alone and therefore, the best result was achieved when combining data from all sensor levels.

Comparing velocity models

In the following section, inversion results obtained employing three different velocity models (NN, KD and local 1D model) are compared. In case of synthetic tests, the same velocity model was applied for both the computation of the synthetic waveforms as well as its inversion. When inverting synthetically computed seismograms, the source mechanism was retrieved equally well independent of which velocity model was employed (Kühn et al., 2020). However, when inverting the observed data, results differed depending on the velocity model. In any case, a 1 km shift of the epicentral location towards south from its public catalogue location was observed (Fig. 9, top). This shift was also recognised by Willacy et al. (2019) and was confirmed by an event relocation using the EDT method (Spetzler and Dost, 2017).

Only for the local 1D model, best and mean solution were fully consistent in the Hudson plot (Fig. 9, bottom). In addition, the variation in CLVD component was smallest and only allowed for positive signs. Inversions employing this model also resulted in the most consistent hypocentral locations, with the event depth of 3 km fitting the reservoir depth. For both NN and KD model, event depths were either more shallow or larger (and thus outside the reservoir layer). For the KD model, epicentral locations are more ambiguous. Fig. 10 presents a comparison of observed and modelled waveforms for sensor G172 at a depth of 100 m, an epicentral distance of 8.2 km and an azimuth of approximately 95°.

Although we display the results in terms of P-phase waveforms in order to be more easily comparable, results were derived from three different types of input data: waveforms (Fig. 10a), amplitude spectra (Fig. 10b) and cross-correlation traces (Fig. 10c). The amplitudes of the traces are scaled according to the target weight and normalised relative to the maximum amplitude of the targets of the corresponding normalisation family (i.e. P-phase waveforms, P-phase amplitude spectra and P-phase cross-correlation traces). Fig. 10 (bottom) displays the moment tensors and their decomposition. In terms of moment tensor solution, the CLVD component had a similar orientation for NN and local 1D model. The DC component, however, showed strike-slip faulting for both NN and KD model, but normal faulting on a steeply dipping fault for the local 1D model, which is in accordance with mechanisms found earlier in the field by Kraaijpoel and Dost (2013).

Full moment tensor

As was the case when inverting synthetically computed seismograms for a deviatoric moment tensor assuming a deviatoric mechanism as source, the source mechanism was again retrieved well when inverting modelled seismograms for a full moment tensor assuming a source including a volumetric component, independent of the velocity model employed (Kühn et al., 2020). When comparing the waveform fit for the inversions of observed data for deviatoric and full moment tensor, the overall fit of waveforms as recognisable by eye is similar (Fig. 11). In addition, a similar shift in event location was observed as when inverting for a deviatoric moment tensor (Fig. 12, top).

Although according to the tests employing synthetic data, both NN and KD velocity model should be able to resolve a full moment tensor, solutions were very unstable as recognisable in both event locations and Hudson diagram (Fig. 12, top and middle). Whereas the isotropic component indicated a volume expansion when the NN or KD velocity model was assumed, it was negative in case of the 1D local velocity model amounting to -20%, agreeing to expectations in case of an event occurring within a depleted reservoir. Both in space as well as in the Hudson diagram, solutions were tightly clustered, suggesting that the retrieved moment tensor is more stable as for the NN and KD velocity models. This was also suggested by the fact that best and mean solution (Fig. 12, bottom) were identical and the double couple percentage was higher than the CLVD percentage. Interestingly, the best double couple was similar no matter if inverting for a deviatoric or a full moment tensor when using the local 1D velocity model, but not when employing the NN or KD model.

Stability of solution and influence of noise

A further suite of tests analysed the influence of random complex noise. The frequency spectra of synthetic waveforms W_{syn} were multiplied with a random frequency response $F_{rand}(\sigma)$ drawn from a normal distribution. Thus, phase and amplitude of the synthetic waveforms were distorted to W_{pert}:

$$W_{pert} = W_{syn} \cdot F_{rand}(\sigma). \quad (5)$$

When the standard deviation σ of both real and imaginary part of the random frequency response coefficients was chosen to be < 5, moment tensors were retrieved perfectly, no matter which velocity model was employed or if the inversion was performed for a deviatoric or a full moment tensor (Kühn et al., 2020). In case that the standard deviation amounted to 10, both retrieved moment tensors (Fig. 13, top) as well as event locations deteriorated.

The simpler the velocity model, the more unstable were the event locations. For both KD and local 1D velocity model, uncertainties in epicentre location were similar, but the depth resolution remained better for the local 1D velocity model. for the NN model, event location uncertainties increased further if the inversion was either restricted to a double couple mechanism or allowed for a full moment tensor (Fig. 13, bottom). However, even when a double couple mechanism was enforced, no rotation of the double couple component due to the noise distorting the orientation of fault planes was found, in contrast to the observations by Jechumtálová and Sílený (2005). In addition, for both inversions for a deviatoric and a full moment tensor, the double couple was correctly retrieved in case that either the KD or 1D velocity model was employed.

When we inverted for a deviatoric moment tensor, the noise was mostly mirrored in the CLVD component, which could assume both positive and negative values, the variation being especially high in case that the NN model was chosen. In addition, the magnitude was overestimated, especially when using the NN and KD model.

When we inverted for a full moment tensor (Fig. 13, bottom), the noise was included in an artificial isotropic in addition to the artificial CLVD component, which was largest for the NN and the local 1D model (68% and 55%, respectively). In the Hudson plot, two groups of solutions were recognisable for NN and KD velocity model, whereas solutions formed a band in case of the local 1D velocity model. In case of KD and local 1D model, the cloud of potential mechanisms included the correct solution, whereas for the NN model, there were no solutions featuring only a low artificial isotropic component. Further, we would like to point out that for the local 1D model, the artificial isotropic component was different than the one retrieved during inversion of the data, which strengthens our confidence that the observed isotropic component is not just an artefact from noise, but can be interpreted geomechanically.

Discussion and conclusions

Employing a plethora of tests, we derived rules of good practice for moment tensor inversion of events recorded in the Groningen field. These concern the velocity model employed to compute Green's functions, types of input data, input parameters and geophone depth levels. Further, we tested the resolvability of different mechanisms, the influence of noise and compared inversions for deviatoric and full moment tensors. Especially during such tests, the advantages of applying a probabilistic inversion become apparent. A regular inversion may lead to the same solution, but its uncertainties and alternative models are largely obscure, whereas probabilistic methods allow for extraction of a range of nearly equivalent source mechanisms, such that parameter trade-offs, uncertainties and ambiguities can be analysed. In our opinion, performing tests to gain an insight of how input data and parameter settings influence the outcome of a moment tensor inversion are a vital prerequisite for understanding and interpreting its results.

A great advantage of the bootstrap method employed here over other approaches in error propagation is that it implicitly accounts for modelling errors that may affect every station and phase differently (Dahm et al., 2018). The assessment of velocity models, though, has to be considered as inherently incomplete, since only a finite number of models can be tested. Instead of varying a single model, we preferred to compare results for widely different models that have been or are currently applied within the region of interest. In addition, our approach employing pre-computed Green's functions data bases opens the possibility to simulate ground motions for earthquake scenarios as was demonstrated by Dahm et al. (2018).

Due to our analysis, we are confident that the isotropic component observed during inversion for the full moment tensors is real; a geological interpretation, however, will be supported by the computation of source mechanisms of several events. The above mentioned rules of good practice were adopted by KNMI in order to compute full moment tensors of all events with magnitude $M_L \geq 2$ from January 2016 to August 2019 (Dost et al., 2020, this issue). A few parameters had to be adjusted due to practicality. Their paper also includes a discussion of results and a comparison to the placement and characteristics of known faults.

The most important results of our analysis are:

- When computing synthetic data systematically changing the source mechanism, there were a few mechanisms, whose magnitude was not resolved well. However, this was only the case when the source was located within the basal anhydrite layer. Employing forward modelling, we proved that indeed both the original and the retrieved mechanism led to similar waveforms recorded at the receivers. This problem can potentially be solved by inverting for the source tensor instead of the moment tensor.

- Local 1D velocity models give more consistent results than employing either the Northern Netherlands model employed for event location for all of Northern Netherlands or the Kraaijpoel and Dost (2013) model. Such locally adapted velocity models have to be re-computed for each event that is inverted.

- For the case of the Groningen field, a good combination of input parameters seems to consist of time traces (allowing for a shift), cross-correlation traces and amplitude spectra. The fact that a combination of input data is helpful in moment tensor inversion is not new, but its consequences can only be illustrated using a probabilistic method.

- At depth, interference of up- and down-going waves leads to notches in the amplitude spectra at certain frequencies, which can partly remove source information when using narrow frequency bands. The detrimental effect of these notches is overcome by including data recorded at multiple depth levels.

- For all velocity models and combinations of input data tested, a shift in location of 1 km to the south was observed compared to the KNMI induced seismicity catalogue location. Enhanced event locations have important implications for relating earthquakes with known faults within the Groningen field.

- When including random noise in the synthetic tests, both moment tensors and event locations deteriorated. Noise mostly influences the estimates of CLVD components and magnitudes. The orientation of the double couple component was stable, also when enforcing a double couple solution during inversion. When allowing for a full moment tensor in addition, for the local 1D model, the noise was reflected in an artificial isotropic component that is different from the one that was obtained during full moment tensor inversion of the data.

- When solving for a full moment tensor using the local 1D velocity model, isotropic components were negative and the solution can be interpreted as normal fault and collapse at reservoir level.

Data and Resources

We downloaded the data used in the analysis from the publicly available KNMI data portal at `http://rdsa.knmi.nl/dataportal` (last accessed May 2017) (KNMI, 1993). The Python-based inversion code Grond and its description can be found at `https://pyrocko.org/grond/` (last accessed June 2020). Green's functions databases were computed with the Python Pyrocko-GF software library residing at `https://pyrocko.org/` (last accessed June 2020). The Green's function databases can be downloaded from the Pyrocko Green's Mill at `https://greens-mill.pyrocko.org`(last accessed June 2020). All inversion runs including parameter files and complete set of check and result plots are available from `https://data.pyrocko.org/scratch/grond-reports/groningen/` (Kühn et al., 2020). The 3D velocity model (Romijn, 2017) is available from NAM (Nederlandse Aardolie Maatschappij) on request.

Acknowledgments

We are grateful to Nederlandse Aardolie Maatschappij (NAM) for providing the complete data to construct the 3D velocity model, from which the local 1D models are extracted, and for valuable insight into the Groningen field. Further, we would like to thank L. Zühlsdorff for actually building the 3D ray tracing model and extracting countless 1D models for us. The authors are thankful to the editor and two anonymous reviewers who provided comments that greatly improved the manuscript. This project has been funded by Gassnova as part of the CLIMIT-demo research program – the Norwegian national program for research, development, and demonstration of CO_2 capture and storage technology (project 242007: "Assessing the capabilities of induced seismicity monitoring for CO_2 storage"). M. P. Isken thanks Dr. Henriette Sudhaus and acknowledges funding by the German Research Foundation DFG through an Emmy Noether Young Researcher Grant (no. 276464525: "Brückenschlag zwischen Geodäsie und Seismologie zur verbesserten und automatisierten Untersuchung von Bruchvorgängen").

References

Alvizuri, C., Silwal, V., Krischer, L., and Tape, C. (2018). Estimation of full moment tensors, including uncertainties, for nuclear explosions, volcanic events, and earthquakes. *J. Geophys. Res. B Solid Earth Planets*, 123(6):5099–5119.

Cesca, S., Heimann, S., Kriegerowski, M., Saul, J., and Dahm, T. (2017). Moment tensor inversion for nuclear explosions: what can we learn from the 6 January and 9 September 2016 nuclear tests, North Korea? *Seismol. Res. Lett.*, 88(2A):300–310.

Dahm, T., Heimann, S., Funke, S., Wendt, S., Rappsilber, I., Bindi, D., Plenefisch, T., and Cotton, F. (2018). Seismicity in the block mountains between Halle and Leipzig, Central Germany: centroid moment tensors, ground motion simulation, and felt intensities of two M $\approx$ 3 earthquakes in 2015 and 2017. *J. Seismol.*, 22(4):985–1003.

Dando, B., Oye, V., Näsholm, S., Zühlsdorff, L., Kühn, D., and Wuestefeld, A. (2019). Complexity in microseismic phase identification: full waveform modelling, traveltime computations and implications for event locations within the Groningen gas field. *Geophys. J. Int.*, 217(1):620–649.

Daniel, G., Fortier, E., Romijn, R., and Oates, S. (2016). Location results from borehole microseismic monitoring in the Groningen gas reservoir, Netherlands. In *Sixth EAGE Workshop on Passive Seismic*. European Association of Geoscientists & Engineers.

de Jager, J. and Visser, C. (2017). Geology of the Groningen field–an overview. *Geol. Mijnbouw*, 96(5):s3–s15.

Dost, B. and Kraaijpoel, D. (2013). The August 16, 2012 earthquake near Huizinge (Groningen). Technical report, KNMI.

Dost, B., Ruigrok, E., and Spetzler, J. (2017). Development of seismicity and probabilistic hazard assessment for the Groningen gas field. *Geol. Mijnbouw*, 96(5):s235–s245.

Dost, B., van Stiphout, A., Kühn, D., Kortekaas, M., Ruigrok, E., and Heimann, S. (2020). Probabilistic moment tensor inversion for hydrocarbon-induced seismicity in the Groningen gas field, the Netherlands, part 2: application. *Bull. Seism. Soc. Am.*

Duputel, Z., Rivera, L., Fukahata, Y., and Kanamori, H. (2012). Uncertainty estimations for seismic source inversions. *Geophys. J. Int.*, 190(2):1243–1256.

Efron, B. (1979). Bootstrap methods: Another look at the jackknife. *Ann. Statist.*, 7(1):1–26.

Fichtner, A. and Simutė, S. (2018). Hamiltonian monte carlo inversion of seismic sources in complex media. *J. Geophys. Res. B Solid Earth Planets*, 123(4):2984–2999.

Gu, C., Marzouk, Y. M., and Toksz, M. N. (2017). Waveform-based Bayesian full moment tensor inversion and uncertainty determination for the induced seismicity in an oil/gas field. *Geophys. J. Int.*, 212(3):1963–1985.

Heimann, S. (2011). *A robust method to estimate kinematic earthquake source parameters*. PhD thesis, University of Hamburg, Germany.

Heimann, S., Isken, M., Kühn, D., Sudhaus, H., Steinberg, A., Vasyura-Bathke, H., Daout, S., Cesca, S., and Dahm,

T. (2018). Grond - A probabilistic earthquake source inversion framework. http://doi.org/10.5880/GFZ.2.1.2018.003. http://pyrocko.org/grond/docs/current/.

Heimann, S., Kriegerowski, M., Isken, M., Cesca, S., Daout, S., Grigoli, F., Juretzek, C., Megies, T., Nooshiri, N., Steinberg, A., et al. (2017). Pyrocko - An open-source seismology toolbox and library. http://doi.org/10.5880/GFZ.2.1.2017.001. http://pyrocko.org.

Heimann, S., Vasyura-Bathke, H., Sudhaus, H., Isken, M., Kriegerowski, M., Steinberg, A., and Dahm, T. (2019). A python framework for efficient use of pre-computed Green's functions in seismological and other physical forward and inverse source problems. *Solid Earth*, 10(6):1921–1935.

Hofman, L., Ruigrok, E., Dost, B., and Paulssen, H. (2017). A shallow seismic velocity model for the Groningen area in the Netherlands. *J. Geophys. Res. B Solid Earth Planets*, 122(10):8035–8050.

Hudson, J., Pearce, R., and Rogers, R. (1989). Source type plot for inversion of the moment tensor. *J. Geophys. Res. B Solid Earth Planets*, 94(B1):765–774.

Jechumtálová, Z. and Sílený, J. (2005). Amplitude ratios for complete moment tensor retrieval. *Geophys. Res. Lett.*, 32(22).

KNMI (1993). Netherlands seismic and acoustic network. `https://`

doi.org/10.21944/e970fd34-23b9-3411-b366-e4f72877d2c5. Royal Netherlands Meteorological Institute (KNMI).

Kraaijpoel, D. and Dost, B. (2013). Implications of salt-related propagation and mode conversion effects on the analysis of induced seismicity. *J. Seismol.*, 17(1):95–107.

Kühn, D., Heimann, S., Isken, M. P., Ruigrok, E., and Dost, B. (2020). Moment tensor inversion testing report on hydrocarbon-induced seismicity in the Groningen gas field, the Netherlands. http://doi.org/10.5880/GFZ.2.1.2020.003. https://data.pyrocko.org/scratch/grond-reports/groningen/.

Li, J., Kuehl, H., Droujinine, A., and Blokland, J.-W. (2016). Microseismic and induced seismicity simultaneous location and moment tensor inversion: Moving beyond picks with a robust full-waveform method. In *SEG Technical Program Expanded Abstracts 2016*, pages 2535–2539. Society of Exploration Geophysicists.

Li, J., Kuleli, H. S., Zhang, H., and Toksöz, M. N. (2011). Focal mechanism determination of induced microearthquakes in an oil field using full waveforms from shallow and deep seismic networksdetermining focal mechanism by waveforms. *Geophysics*, 76(6):WC87–WC101.

Lu, R., Willen, D., and Watson, I. (2003). Identifying, removing, and imaging PS conversions at salt-sediment interfaces. *Geophysics*, 68(3):1052–1059.

Mustać, M. and Tkalčić, H. (2015). Point source moment tensor inversion through a Bayesian hierarchical model. *Geophys. J. Int.*, 204(1):311–323.

Ogilvie, J. and Purnell, G. (1996). Effects of salt-related mode conversions on subsalt prospecting. *Geophysics*, 61(2):331–348.

Paap, B., Kraaijpoel, D., Bakker, M., and Gharti, H. (2018). Wave propagation modelling of induced earthquakes at the Groningen gas production site. *Geophys. J. Int.*, 214(3):1947–1960.

Pickering, M. (2015). An estimate of the earthquake hypocenter locations in the Groningen gas field. Technical report, Nederlandse Aardolie Maatschappij BV.

Romijn, R. (2017). Groningen velocity model 2017 - Groningen full elastic velocity model September 2017. Technical report, Nederlandse Aardolie Maatschappij BV.

Rubin, D. B. (1981). The bayesian bootstrap. *Ann. Statist.*, 9(1):130–134.

Ruigrok, E., Domingo-Ballesta, J., van den Hazel, G.-J., Dost, B., and Evers, L. (2019). Groningen explosion database. *First Break*, 37(8):37–41.

Silver, P. G. and Jordan, T. H. (1982). Optimal estimation of scalar seismic moment. *Geophys. J. Int.*, 70(3):755–787.

Silwal, V. and Tape, C. (2016). Seismic moment tensors and estimated uncertainties in southern alaska. *J. Geophys. Res. B Solid Earth Planetsh*, 121(4):2772–2797.

Spetzler, J. and Dost, B. (2017). Hypocentre estimation of induced earthquakes in Groningen. *Geophys. J. Int.*, 209(1):453–465.

Stähler, S. C. and Sigloch, K. (2014). Fully probabilistic seismic source inversion–part 1: Efficient parameterisation. *Solid Earth*, 5(2).

Tan, Y., Zhang, H., Li, J., Yin, C., and Wu, F. (2018). Focal mechanism determination for induced seismicity using the neighbourhood algorithm. *Geophysical Journal International*, 214(3):1715–1731.

Tape, W. and Tape, C. (2016). A confidence parameter for seismic moment tensors. *Geophysical Journal International*, 205(2):938–953.

Tarantola, A. and Valette, B. (1982). Inverse problems= quest for information. *Journal of Geophysics*, 50(1):159–170.

Wang, R. (1999). A simple orthonormalization method for stable and efficient computation of Green's functions. *Bull. Seism. Soc. Am.*, 89(3):733–741.

Wéber, Z. (2006). Probabilistic local waveform inversion for moment tensor and hypocentral location. *Geophys. J. Int.*, 165(2):607–621.

Willacy, C., van Dedem, E., Minisini, S., Li, J., Blokland, J., Das, I., and Droujinine, A. (2018). Application of full-waveform event location and moment-tensor inversion for Groningen induced seismicity. *The Leading Edge*, 37(2):92–99.

Willacy, C., van Dedem, E., Minisini, S., Li, J., Blokland, J.-W., Das, I., and Droujinine, A. (2019). Full-waveform event location and moment tensor inversion for induced seismicity. *Geophysics*, 84(2):KS39–KS57.

Zahradnik, J., Jansky, J., and Plicka, V. (2008). Detailed waveform inversion for moment tensors of M $\sim$ 4 events: examples from the Corinth Gulf, Greece. *Bull. Seism. Soc. Am.*, 98(6):2756–2771.

List of Figures

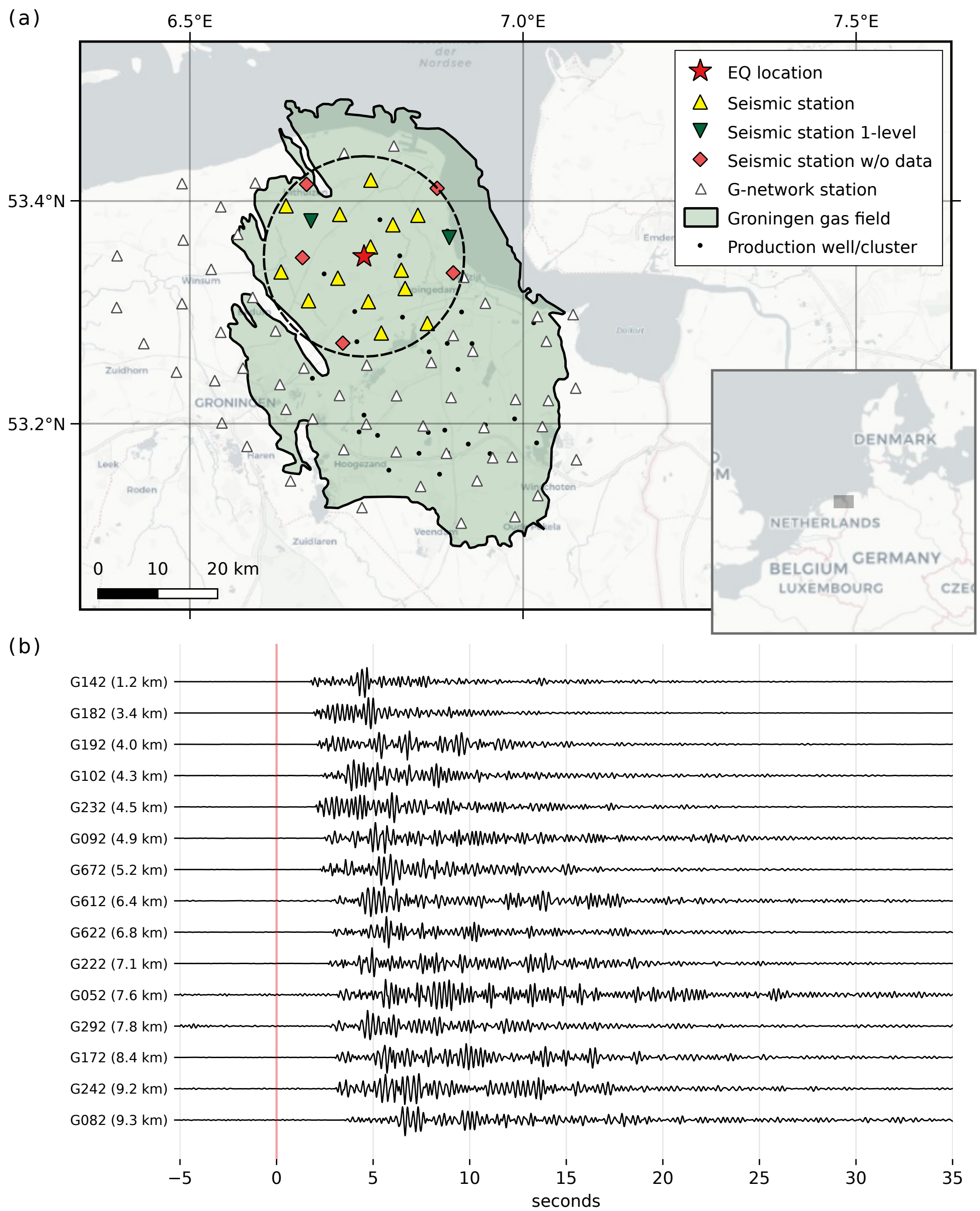

Figure 1: a) Map of study region indicating the location of the 11$^{\text{th}}$ March 2017 event indicated by a star within the Groningen field (shaded). A dotted circle represents a source distance of 10 km; stations are marked by triangles and diamonds. b) Seismograms recorded on vertical components of stations with a source-station distance less than 10 km; data are restituted and filtered between 1 and 4 Hz.

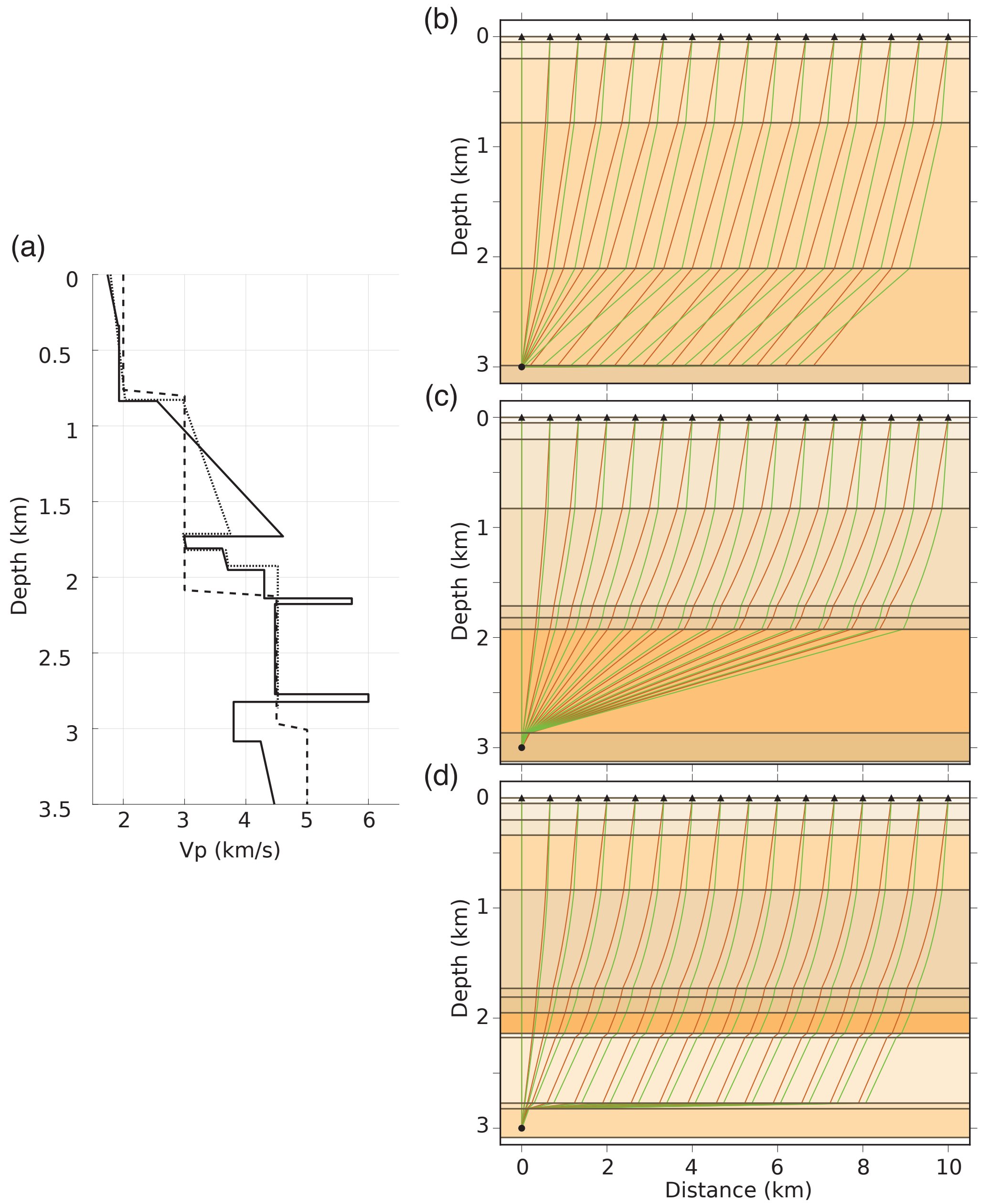

Figure 2: a) Velocity models tested for moment tensor inversion in this paper: NN model (dashed line), KD model (dotted line) and local 1D model (solid line); b) traced rays paths in NN model, c) in KD model and d) in local 1D model.

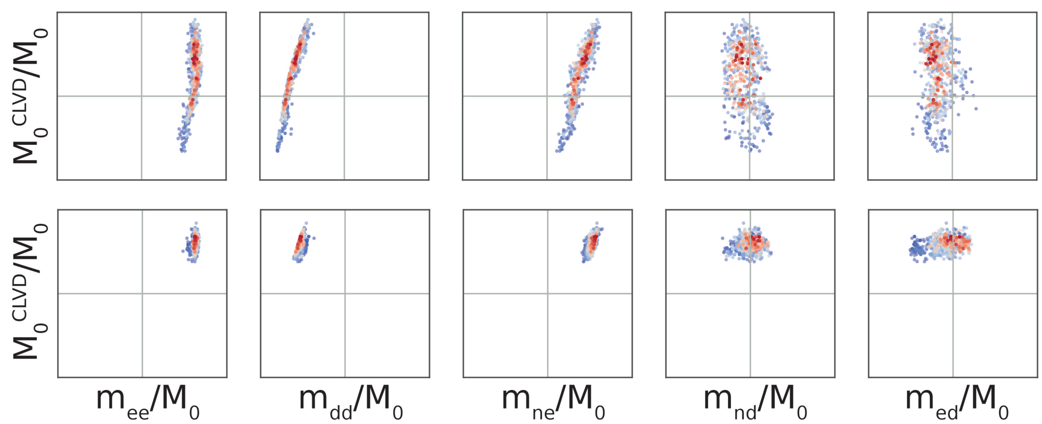

Figure 3: Cross-plots for a selection of inversion parameters demonstrating distribution of result ensemble consisting of 1000 solutions with comparable misfit in parameter space; comparison between inversion of time traces (top) and cross-correlation traces (bottom). Inversion parameters shown comprise the moment of the CLVD part M^{CLVD_0} and several moment tensor components (m_{ee}, m_{dd}, m_{ne}, m_{nd}, m_{ed}; e denoting East, n North and d depth), all scaled according to the total seismic moment M_0. Colour scale according to misfit distribution within ensemble, red/high opacity: low misfit, blue/high transparency: high misfit (offline version: dark tones indicate low misfit, light tones high misfit).

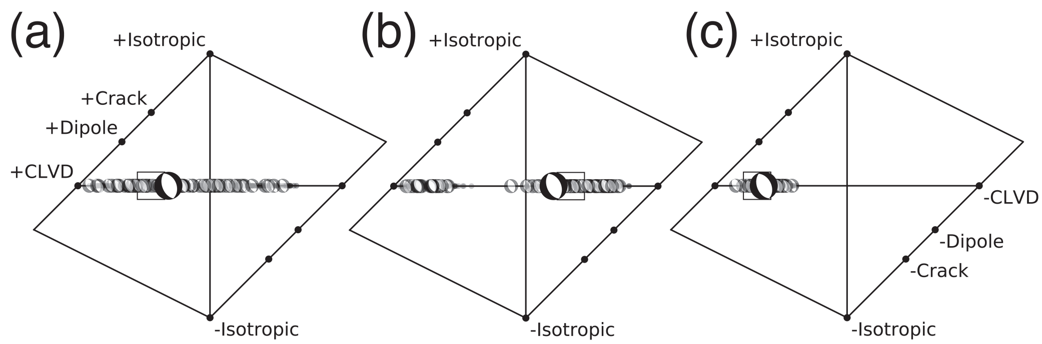

Figure 4: Hudson plots (Hudson et al., 1989) representing the source decomposition for inversions employing different types of input data; a) time traces, b) time traces and amplitude spectra, c) time traces and cross-correlation traces. Best double couple mechanisms (north-east-down coordinate system) are shown for all solutions; the best solution is surrounded by a square and the inflated focal sphere constitutes the mean solution.

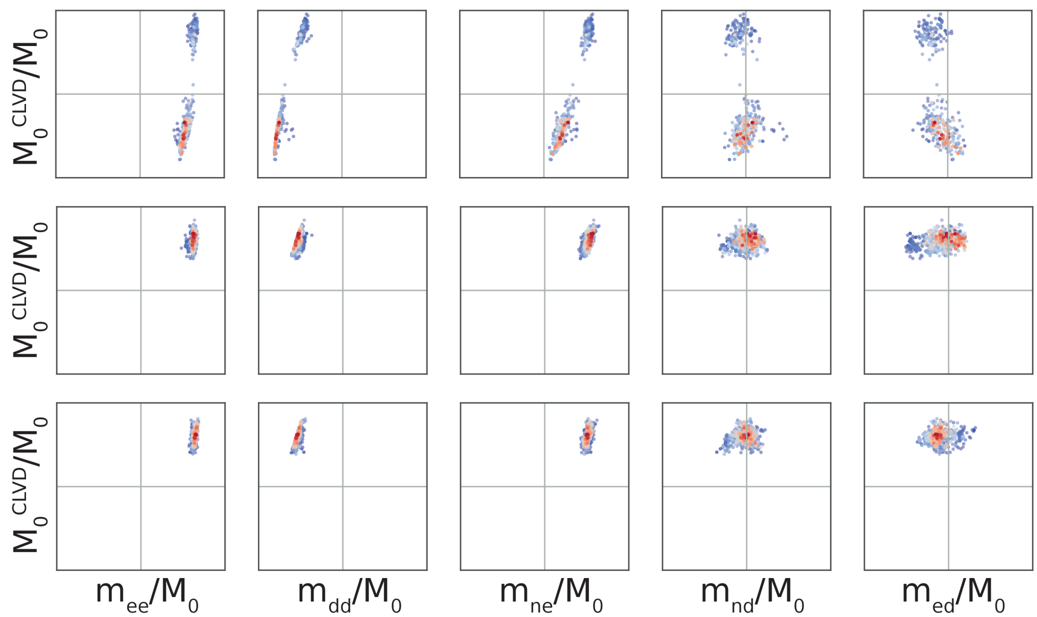

Figure 5: Cross-plots for a selection of inversion parameters demonstrating distribution of solutions with comparable misfit in parameter space; comparison between inversion of a combination of time traces with amplitude spectra (top), time traces with cross-correlation traces (middle) and time traces with amplitude spectra with cross-correlation traces (bottom)

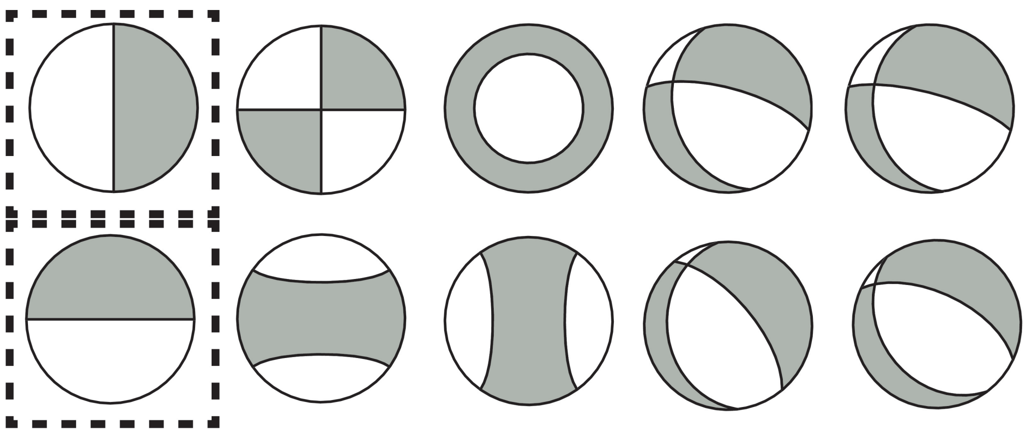

Figure 6: Source mechanisms employed to compute synthetic data for testing the inversion algorithm: three double couple mechanisms, three CLVDs and the four focal mechanisms computed for the Groningen field by Kraaijpoel and Dost (2013); mechanisms marked by a dashed box are found, but assigned an erroneous magnitude

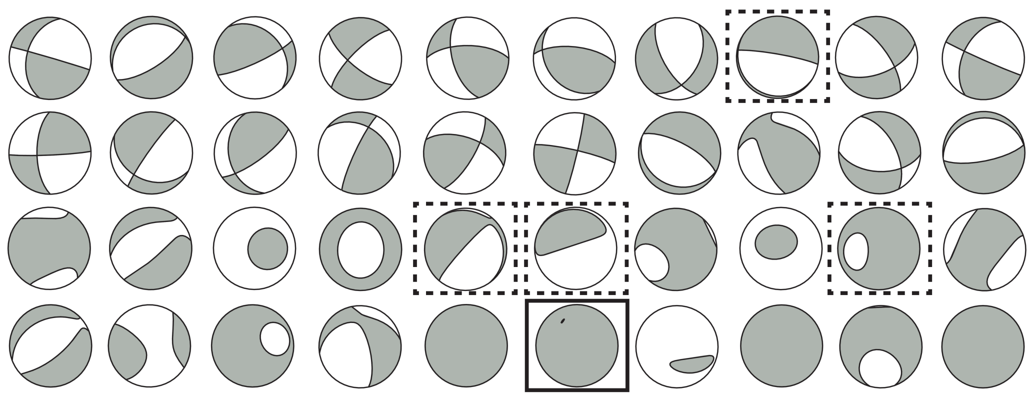

Figure 7: Randomly varied double couple source mechanisms (two top rows) and full moment tensors (two bottom rows); mechanisms marked by an dashed box are found, but assigned an erroneous magnitude and event depth; a faulty solution is assigned to the mechanism marked by the black box

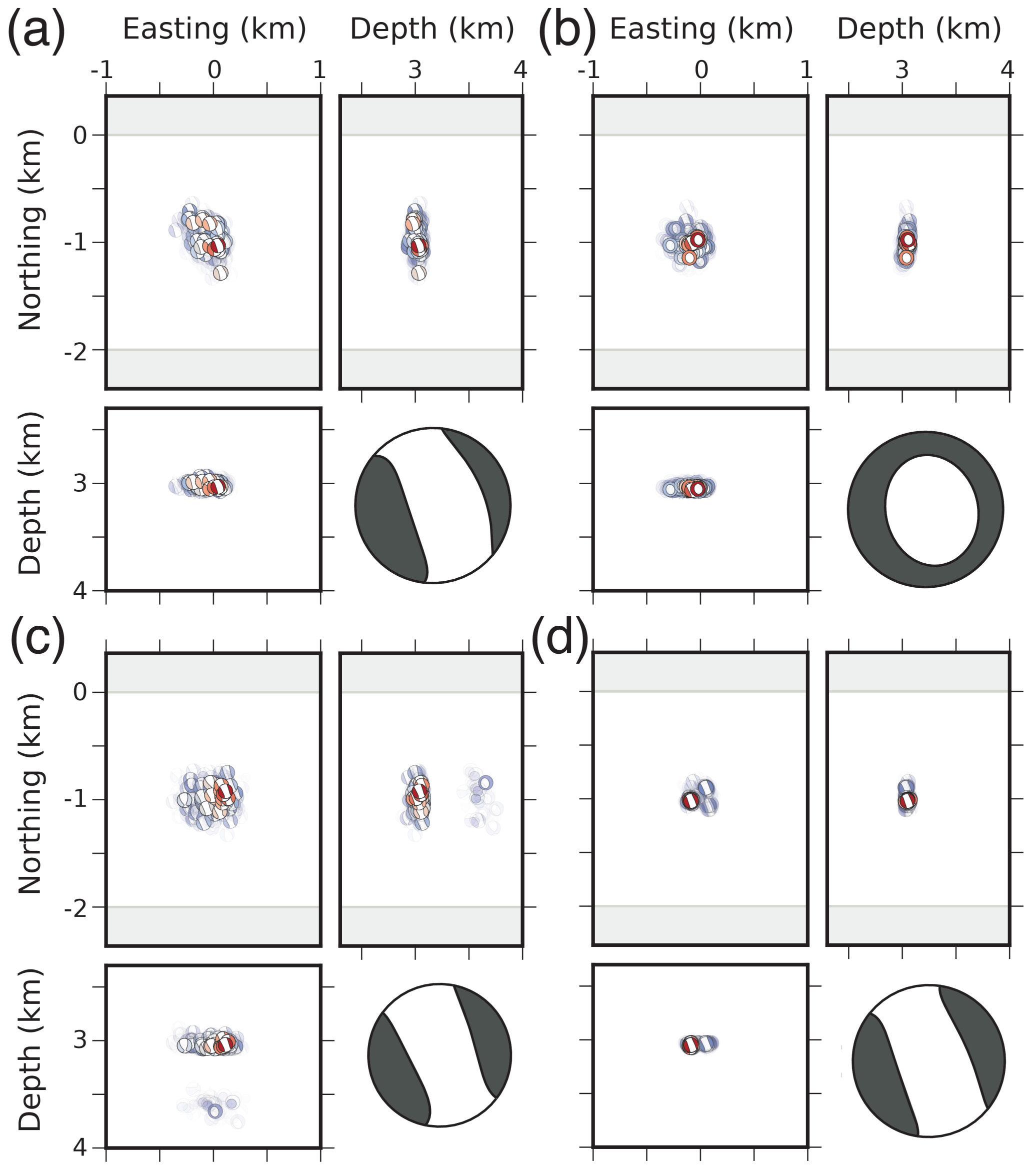

Figure 8: Testing inversions employing data from different depth levels within the borehole: a) sensor at 50 m depth, b) sensor at 150 m depth, c) sensor at 200 m depth, d) combining sensors from all depth levels (50 m, 100 m, 150 m, 200 m). For every test run, the resulting deviatoric moment tensor is shown along with ensemble event locations as map view and depth sections. As for the parameter cross-plots, the colour scale is according to the misfit distribution within the ensemble, red: low misfit, blue: high misfit (offline version: dark tones indicate low misfit, light tones high misfit).

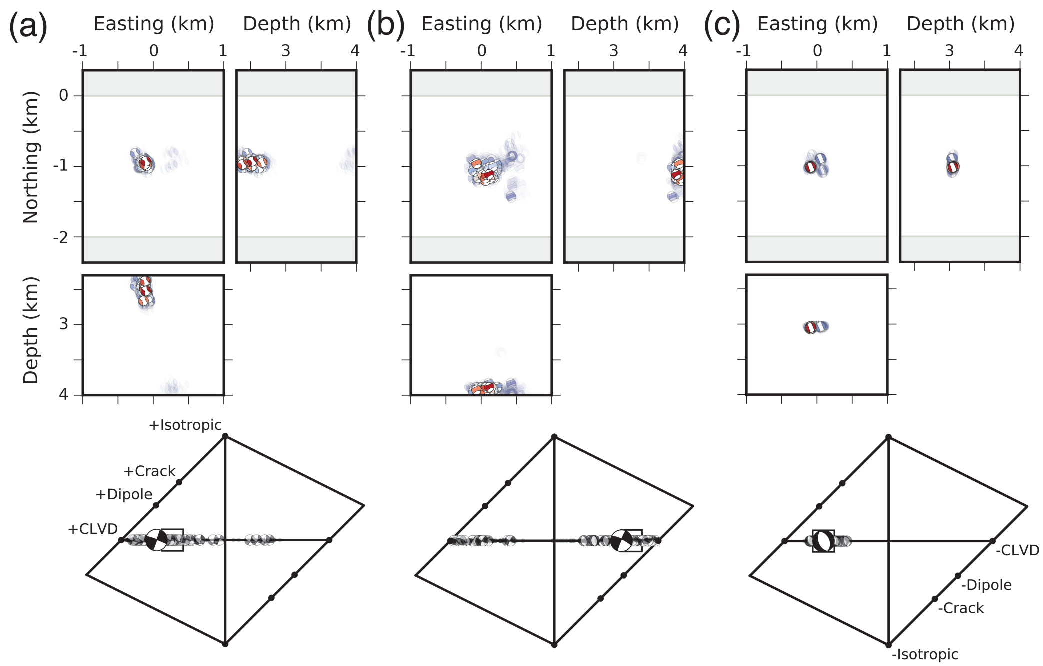

Figure 9: Comparing results for different velocity models; a) NN model, b) KD model, c) local 1D model; top: event locations; bottom: Hudson diagrams displaying best double couple mechanisms

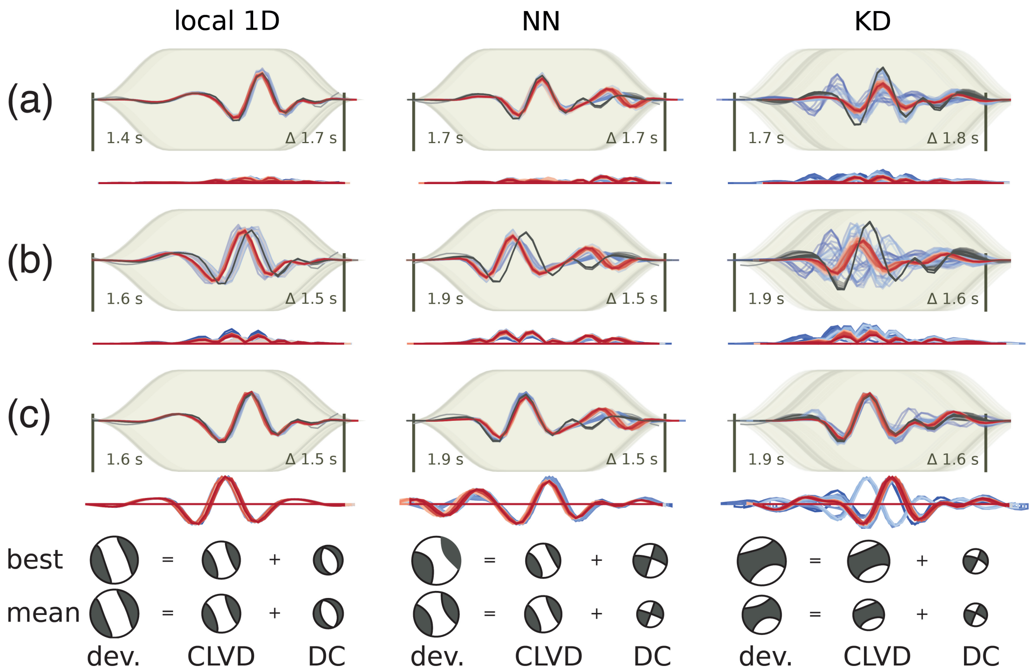

Figure 10: Comparing results for different velocity models (left: local 1D model, middle: NN model, right: KD model). Top three rows: waveform fits and residuals; input data to the inversion were (a) time domain waveforms, (b) amplitude spectra and (c) normalized cross-correlations traces. Thin lines: light grey - restituted and filtered observed traces, dark grey - same trace processed applying a taper (background grey area). Slightly thicker lines: modelled traces. Colors from red to blue indicate low to high misfit of modelled traces to observed traces (offline version: dark tones indicate low misfit, light tones high misfit). Numbers to the left of the taper window indicate starting time of the waveform relative to the event origin time, numbers to the right refer to length of fitted time window. Lines below the taper window indicate sample-by-sample differences between observed and modelled traces (similar colouring), comparable only within each row, not among rows. Bottom row: deviatoric moment tensors and their decomposition. Leftmost focal sphere diagram represents deviatoric moment tensor decomposed into CLVD (middle) and best double couple (right). Size of the focal sphere diagrams indicates their relative scalar moments. Upper row: best solution, lower row: mean solution averaged over 1000 best solutions.

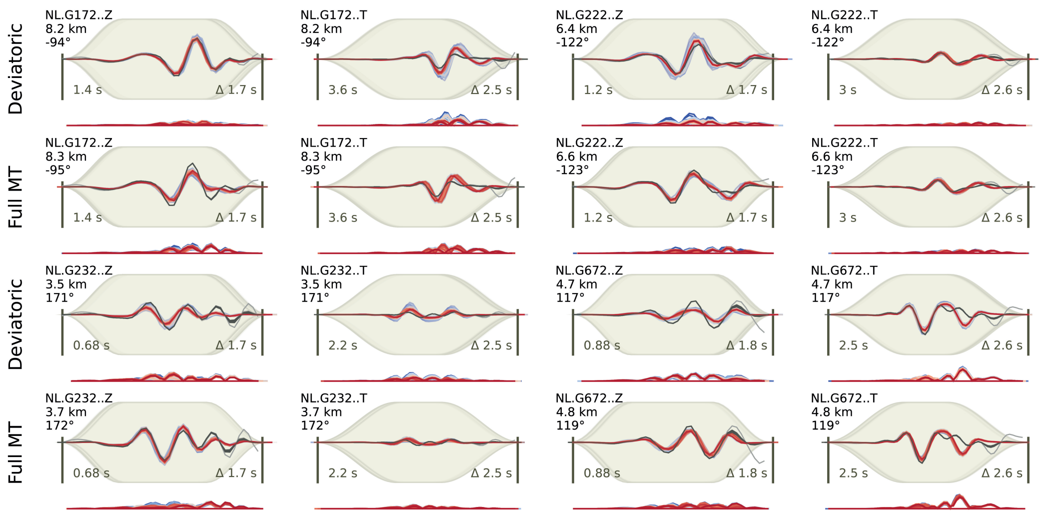

Figure 11: Time domain waveform fits and residuals for deviatoric and full moment tensor inversion compared at sensors G172, G222, G232 and G672, corresponding to level 2 (100 m depth) of stations G17, G22, G23 and G67. For each sensor, vertical and transverse components are shown (denoted by Z and T, respectively) and distance and azimuth with respect to the source is given (detailed description of waveform fit plots available in caption of Fig. 10).

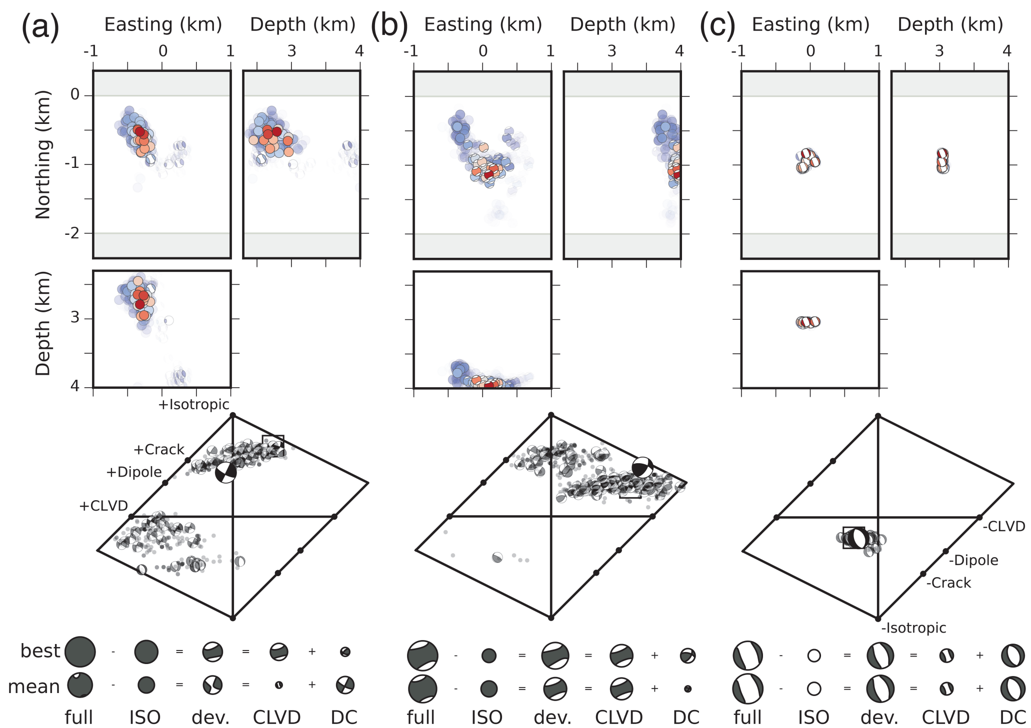

Figure 12: Comparing full moment tensor results for different velocity models: a) NN model, b) KD model, c) local 1D model; top: event locations, middle: Hudson diagrams displaying best double couple mechanisms, bottom: solutions. In addition to deviatoric, CLVD and DC mechanisms, isotropic part and full moment tensor are depicted (two bottom rows).

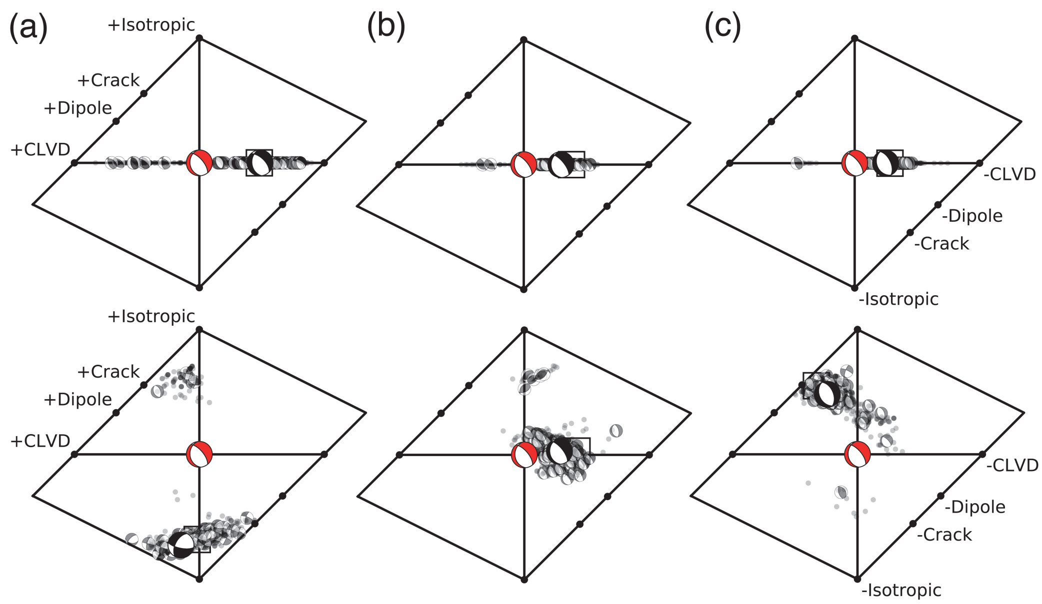

Figure 13: Hudson plots displaying best double couple mechanisms comparing results of inversions of synthetic data including noise for different velocity models: a) NN model, b) KD model, c) local 1D model; top: inversion for deviatoric moment tensor; bottom: inversion for full moment tensor. The focal sphere diagram displayed in the centre represents the double couple employed to compute the synthetic data set.